



Contents lists available at ScienceDirect

Journal of the Mechanics and Physics of Solids

journal homepage: www.elsevier.com/locate/jmps

Conditions controlling kink crack nucleation out of, and delamination along, a mixed-mode interface crack

J. William Pro^a, Stephen Sehr^b, Rone Kwei Lim^c, Linda R. Petzold^d,
Matthew R. Begley^{e,*}

^a Department of Mechanical Engineering, 117 McConnell Engineering Building, McGill University, Montréal, QC H3A 0E9, Canada

^b Department of Mechanical Engineering, 2235C Engineering II Building, University of California, Santa Barbara, CA 93106, USA

^c Department of Computer Science, 5110 Harold Frank Hall, University of California, Santa Barbara, CA 93106, USA

^d Department of Mechanical Engineering and Department of Computer Science, 5107 Harold Frank Hall, University of California, Santa Barbara, CA 93106, USA

^e Materials Department and Department of Mechanical Engineering, 2361A Engineering II Building, University of California, Santa Barbara, CA 93106, USA

ARTICLE INFO

Article history:

Received 23 April 2018

Revised 1 August 2018

Accepted 20 August 2018

Available online 22 August 2018

Keywords:

Fracture mechanics

Cohesive zone modeling

Crack kinking

Interface fracture

ABSTRACT

This paper analyzes the competition between kink nucleation and interface fracture for an interface crack (without a putative kink flaw) subject to mixed-mode loading. The simulations utilize a distributed cohesive zone approach that embeds cohesive elements throughout the entire mesh; dynamic crack path evolution occurs through a loss of cohesive traction associated with a critical separation between elements. The simulations identify mesh densities that lead to mesh-independent results for randomly oriented triangular meshes, and provide clear guidelines regarding parameters that recover toughness-controlled cracking (i.e. linear elastic fracture mechanics). The results demonstrate that, when the normalized bulk toughness is far from the transition between kinking and delamination, crack direction and critical loads are identical to those predicted by He and Hutchinson, who analyzed cracking from a putative flaw associated with the maximum energy release rate. Near the transition between fracture modes, kink nucleation depends on the relative size of the interface and bulk process zones, such that additional criteria are needed (beyond those postulated by He and Hutchinson). Regime maps are presented which indicate regions of kink nucleation versus delamination as a function of controlling cohesive parameters.

© 2018 Published by Elsevier Ltd.

1. Introduction

Kinking from an interface has been studied extensively assuming that a putative flaw exists at the interface to initiate kinking (Azhdari and Nemat-Nasser, 1996; Bilby and Cardew, 1975; Bilby et al., 1978; Hayashi and Nemat-Nasser, 1981; He et al., 1991; He and Hutchinson, 1989b; 1989c; Hutchinson and Suo, 1992; Karihaloo et al., 1980; Lo, 1978; Nuismer, 1975; Wu, 1978a; 1978b; 1978c; 1979). A schematic of a putative kink crack is shown in Fig. 1; a small flaw intersects with a 'parent' interface crack with a much larger crack length. The presence of the putative flaw greatly simplifies the analysis,

* Corresponding author.

E-mail address: begley@engineering.ucsb.edu (M.R. Begley).

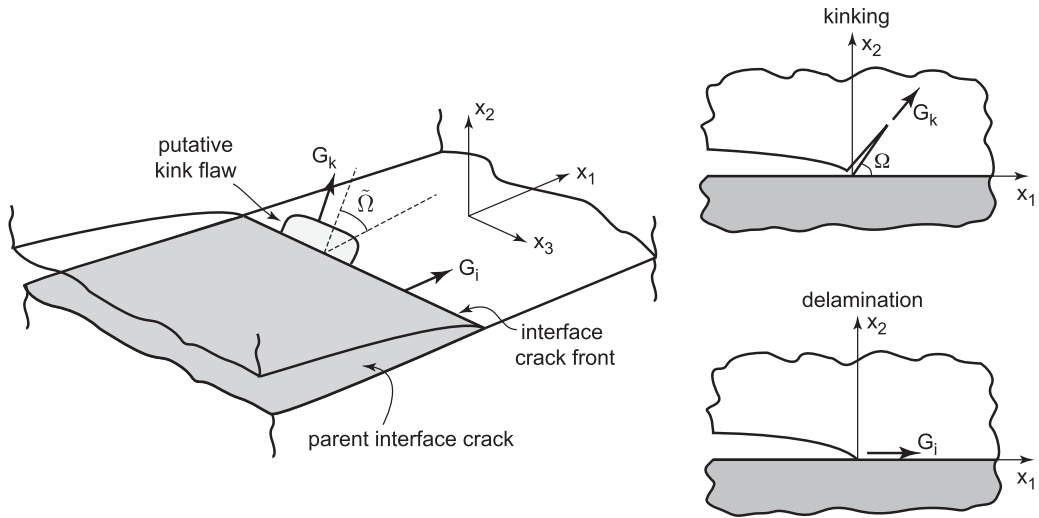


Fig. 1. Schematic of a putative flaw that triggers kinking off of the interface of a bimaterial crack.

essentially by separating the fracture process zones that occur at the tip of the putative kink crack and the parent interface crack. In order for this to be valid, the putative flaw has to be large enough such that its tip is not influenced by any damage at the interface at the base of the kink. This is reasonable for highly brittle solids with rupture zones on the order of 1 – 10 nanometers and flaws on the order of 10–100 nm. The stability of the kink crack is then solely determined by its energy release rate and the bulk material toughness. Put another way, the *a priori* presence of a putative kink flaw avoids the issue of kink *nucleation* by assuming that kink ‘sources’ (i.e. angled putative flaws that intersect the interface) exist wherever they are needed.

In this framework, one must only examine the stability of kink cracks relative to that of the parent crack to determine whether kinking occurs, or remains on the interface. This assumes that the critical driving force for the interface crack is unaffected by the presence of the small kink flaw. This would be the case if the putative kink flaw is present along a small fraction of the interface crack front, as shown in Fig. 1. In such cases, the regions between putative kink flaws are identical to the parent crack and the interface crack’s stability is not influenced by the presence of kink ‘sources’. To apply a two-dimensional, plane strain analysis, one must further assume that the width of the putative kink flaw (measured along the crack front) is much larger than its depth (into the bulk). Put another way, if a substantial portion of the interface crack front is not influenced by putative kink flaws, one does not need to re-nucleate the interface crack ahead of (or beneath) the kink flaw; the region of the crack front between the kink flaws governs continued interface propagation.¹

This reasoning leads to the approach outlined by He and Hutchinson (1989b,c); if the critical condition for interface cracking (absent the putative kink flaw) is reached prior to that for a kink source, interface delamination occurs. Conversely, if the critical condition for advance of the kink flaw occurs prior to that of the interface, the putative kink flaw grows (both in the flaw direction and presumably along the interface). Thus, kinking occurs when:

$$\frac{G_k(\psi)}{\Gamma_b} > \frac{G_i}{\Gamma_i(\psi)} \quad \text{or} \quad \frac{G_k(\psi)\Gamma_i(\psi)}{G_i\Gamma_b} > 1 \tag{1}$$

where G_k is the maximum driving force associated with a putative kink crack (over all possible kink angles, $\tilde{\Omega}$) growing into the bulk material with toughness Γ_b , and G_i is the driving force for cracking along an interface with toughness Γ_i . The phase angle ψ defines the mode-mix for the parent crack, and the above reflects that the driving force for the kink angle that maximizes energy release rate depends on the far-field mode-mix. The interface toughness, $\Gamma_i(\psi)$, may depend on mode-mix as well. Solutions for $G_k(\psi)/G_i$ are tabulated by He and Hutchinson (1989b,c) for two-dimensional geometries (i.e. plane strain and plane stress). This criteria has been validated for some material systems with mixed-mode fracture experiments, involving digital image correlation (Abanto-Bueno and Lambros, 2005; 2006; Kimberley and Lambros, 2004), special purpose interface fracture specimens (e.g., Brazil nut Kang, 1994), and detailed combinations of experiments and finite element simulations (Prasad and Carlsson, 1994a; 1994b).

In the subsequent work of He and Hutchinson (1989a), a similar approach was applied using LEFM to analyze the problem of deflection vs. penetration of an impinging interface crack. It is important to emphasize that, while these two works implement a similar method of putative kink crack analysis, they analyze two fundamentally different cracking scenarios. In the first work (He and Hutchinson, 1989b; 1989c), the crack path selection is part of the problem: the crack can kink out

¹ An alternative explanation for the continued propagation of the interface crack in the presence of kink flaws relates to dynamic instability: if the interface crack grows unstably prior to encountering a kink, dynamic effects could carry the interface flaw past the kink.

of the interface and therefore the kink angle is part of the solution. In their subsequent work (He and Hutchinson, 1989a), the possible crack paths are determined a priori: the crack can only penetrate into the substrate or deflect at a pre-defined angle into the interface. The latter problem is not analyzed here, but has been analyzed by Strom and Parmigiani (2014), and Parmigiani and Thouless (2006) using an intrinsic cohesive zone framework

The later work of He et al. (1991) also implemented the putative kink crack methodology to analyze the role of non-zero T-stress. Here, the authors introduce the dimensionless in-plane stress $\bar{\Gamma}$ and directly illustrate its effect on the relative maximum ERR as a function of the phase angle for both compressive ($\eta < 0$) and tensile ($\eta > 0$) regions. In the compressive region, the in-plane stress tends to suppress kinking via crack closure, and conversely in the tensile region the in-plane stress tends to promote kinking over interface delamination. The effect of non-zero T-stress is beyond the scope of this paper but is left as future work.

The framework by He and Hutchinson (1989b,c) makes three key assumptions: (i) putative kink flaws, or kink sources, exist wherever they are needed, (ii) kink sources along the interface crack front are distributed such that they do not alter the criteria for interface advance, and (iii) damage at the interface near a kink does not alter the driving force for kinking. This last assumption relates to the process zone associated with the interface; it must be much smaller than the size of the putative kink, such that it does not alter the elastic fields at the tip of the interface crack. In the glass-epoxy interface studied by Liechti and Chai (1991), kinking was presumably suppressed because the damage zone in the epoxy was larger than kink flaws in the glass, effectively shielding their tips. For the exceedingly small damage zones in completely brittle systems, this presumably is not a concern, supporting the notion that Eq. (1) is sufficient to decipher crack path selection.

In this work, we relax these assumptions by examining the conditions for kink crack nucleation, i.e. the possibility that a kink crack emerges from a sharp interface crack in the absence of a putative flaw. By using different cohesive laws for the bulk and for the interface, we naturally introduce interactions between process zones at the interface and in the bulk, capturing the influence of partial interface decohesion on kinking. In the simulations, the direction of kinking emerges naturally as a consequence of cohesive elements distributed throughout the bulk material as well as the interface.

In general, the cohesive zone model acts as an approximation to the nonlinear processes ahead of the crack tip (Dugdale, 1960). Unfortunately, an explicit atomistic study of kink nucleation would not be tractable, as the size of the fracture process zone in an ordinary brittle material is on the order of tens of nanometers. Assuming an alumina film with $E = 300$ GPa, bond rupture strength $\sigma_0 = 10$ GPa, and $\Gamma_i = 10$ J/m², one computes the fracture process zone size to be ~ 30 nm. In contrast, the length scale of the macroscopic elastic field that drives deformation (i.e. that establishes the surrounding K field) on this scale is orders of magnitude larger; for example, the controlling length-scale for the K field in coating problems scales with the square root of the coating thickness. Thus, the problem is inherently multiscale. To accurately capture the physics of fracture, the minimum required numerical discretization would have to be on a length scale smaller than the fracture process zone, and span several orders of magnitude to capture deformation at the scale of the film thickness.

As will be shown, many of the calculations in this paper involved a cohesive strength that is about five times lower than an atomistic bond rupture strength in a brittle material, which effectively enlarges the fracture process zone and makes the calculation manageable. While this is not truly representative of brittle fracture processes, it is indeed quite reasonable for quasi-brittle systems with larger process zones occurring on the order of hundreds of nanometers to microns. In these types of systems, the process zones would interact during the transition between kinking and delamination. Near the transition, it would be expected that a small to moderate amount of damage occurs in the bulk prior to delamination which would contribute to the interface toughness and vice versa.

2. Review of related simulations

A number of alternative numerical methods have been developed to simulate non-planar crack growth at coarser length scales *without the assumption/inclusion* of an initial putative flaw (e.g. Augmented FEM, Extended FEM). These methods have proven useful when carefully combined and calibrated with results of mixed-mode fracture experiments (Bayesteh and Mohammadi, 2013; Kumar et al., 2015; Liu et al., 2014; 2013; Motamedi and Mohammadi, 2012; Pathak et al., 2013; Rabczuk et al., 2008), with applications ranging from interfacial fracture in polymer-matrix composites, deformation in welded joints (Cavalli et al., 2004; 2005), and cracking in advanced multilayer systems (Białas et al., 2005; Nekkanty et al., 2007). These approaches require external kinking and growth criteria to be supplied in advance. On the contrary, methods such as cohesive zone models (Xie and Waas, 2006; Xu and Needleman, 1994), peridynamics (De Meo et al., 2016; Gerstle et al., 2007; Han et al., 2016; Madenci and Oterkus, 2014; Silling, 1998; Silling and Lehoucq, 2008; Zhu and Zhao, 2016), and phase field models (Borden et al., 2012; Miehe et al., 2010) do not require an external growth criteria; rather, the failure criteria is intrinsically built into the method. While the latter methods have been shown to qualitatively capture experimental observations of non-planar crack growth (Hakim and Karma, 2009; Madenci et al., 2016), a clear definition of kink nucleation conditions for each method in terms of the local crack tip parameters has yet to be established.

Of particular relevance to modeling non-planar crack evolution is the recent work of Strom and Parmigiani (2014), which builds off the earlier work of Parmigiani and Thouless (2006) as well as Foulk et al. (2008). In these works, the authors model a bi-layer film/substrate specimen with a vertical channel crack impinging at the interface (e.g., perpendicular to the interface). Cohesive elements are placed along the interface and the plane associated with straight penetration into the substrate, and the dimensionless toughness and strength ratio of the cohesive law is parameterized.

In the early work of [Parmigiani and Thouless \(2006\)](#), the authors examine the specific criteria for substrate penetration versus deflection into the interface (initially with no putative kink flaw), in terms of the relative bulk-to-interface strength and toughness ratios. Through large parameter studies, they conclude that the specific nature of the impinging crack penetrating into the substrate or deflecting into the interface must depend on both the strength of the cohesive law, as well as the toughness. In the appendix of this work, the authors take the analysis a step further and explicitly include kink flaws. With highly refined meshes and kink flaws that are much smaller than any physical length in the problem, the authors illustrate that the critical driving force for deflection or penetration converges to the values predicted by [He and Hutchinson \(1989a\)](#).

In the subsequent work ([Strom and Parmigiani, 2014](#)), the authors continue the analysis and consider the critical driving forces for the case without a kink crack (in addition to the parameters controlling deflection/penetration selection) to extend or deflect the penetrating crack. In this work, results are shown for the normalized critical applied stress for either penetration or deflection as a function of the strength and toughness ratio. The theoretical result for the critical load for penetration is derived using LEFM analysis for the bimaterial strip, and the theoretical load for deflection is derived using the putative kink energy based analysis of [He and Hutchinson \(1989a\)](#). Both theoretical curves are plotted simultaneously with the results from the cohesive zone models. It is illustrated that, when the criteria for deflection is satisfied, and is far from the deflection-to-penetration transition, the critical driving force for the deflecting crack asymptotically approaches the energy-based predictions established by [He and Hutchinson \(1989a\)](#).

Conversely, near the transition, the authors show that the critical load is elevated due to interacting process zones along the bulk and interface that require additional energy to drive cracking. The authors confirm the notion in [Parmigiani and Thouless \(2006\)](#) that both stress and energy play a role in the criteria for distinguishing penetration vs. deflection in cohesive zone models where a kink is not initially included. These works can be considered pioneering work relating to crack nucleation, in that they (i) bridge the gap between stress based models ([Cook and Gordon, 1964](#); [Gupta et al., 1992](#)) and energy based models ([He and Hutchinson, 1989a](#)) and (ii) illustrate that the critical driving force for deflection based on energetic predictions of a small kink crack may indeed be recovered without an inclusion of a kink flaw, provided the conditions are far from the transition between deflection and penetration. We again emphasize that neither of the models in [Strom and Parmigiani \(2014\)](#) and [Parmigiani and Thouless \(2006\)](#) recover the criteria for transition between penetration and deflection based on energy alone as in [He and Hutchinson \(1989a\)](#), but [Strom and Parmigiani \(2014\)](#) illustrates that the critical driving force for deflection may be captured in certain limits of cohesive zone analysis without the inclusion of a putative flaw.

The objective of the current work is to unify previous works for predicting crack deflection with similar simulations that capture crack kinking out of the interface. Here, rather than restricting the crack path to two orthogonal crack planes, arbitrary kinking directions are captured by inserting cohesive zones in between all element pairs within an unstructured Delaunay triangulation mesh. In one sense, the approach is a generalization of the works of [Parmigiani and Thouless \(2006\)](#) and [Strom and Parmigiani \(2014\)](#) to predict *arbitrary kinking directions* for a wide range of mode mix and toughness mismatch. By exploiting modern parallel computing platforms and a highly optimized explicit time stepping code, we conduct broad parameter studies to identify the requirements on mesh resolution, quantify the role of cohesive parameters, and establish an efficient set of criteria for crack path evolution.

3. Simulation framework

The simulation framework consists of an explicit dynamic finite element implementation, with rate-independent cohesive elements embedded between all elements in the mesh. It is essentially identical to the method pioneered by [Xu and Needleman \(1994\)](#), with the exception of the description of the cohesive constitutive behavior. For small displacements relative to the cohesive separation parameter, the implementation fully recovers conventional continuum elasticity. Similar frameworks have been widely used to study fracture initiation and growth, albeit with cohesive elements limited to pre-defined crack paths ([Blackman et al., 2003](#); [Borg et al., 2002](#); [El-Sayed and Sridharan, 2002](#); [Hamitouche et al., 2008](#); [Harper and Hallett, 2008](#); [Needleman, 1990a](#); [1990b](#); [Tvergaard, 1990](#); [Tvergaard and Hutchinson, 1992](#)). This requires that the crack path be known in advance, either by experimental measurement or by nature of the structure (e.g., material interfaces). Here, we apply a more general strategy and generate meshes using an unbiased, unstructured Delaunay mesh with cohesive zones distributed at all element pairs (similar to the work found in [Camacho and Ortiz \(1996\)](#); [Xu and Needleman \(1994\)](#) and [Geubelle and Baylor \(1998\)](#)). In this approach, a non-interfacial crack does not ever follow a perfectly straight path, as any crack trajectory is limited to pre-defined element boundaries; the consequences of this are examined closely in the results section.

The remainder of the paper is organized as follows: [Section 3.1](#) outlines the cohesive law and problem geometry, while details regarding the controlling length-scales and numerical implementation are given in [Section 3.2](#); the ensuing parameter study is guided by the dimensional analysis presented in [Section 3.3](#). Results and related discussion are in [Section 4](#), while key conclusions are summarized in [Section 5](#).

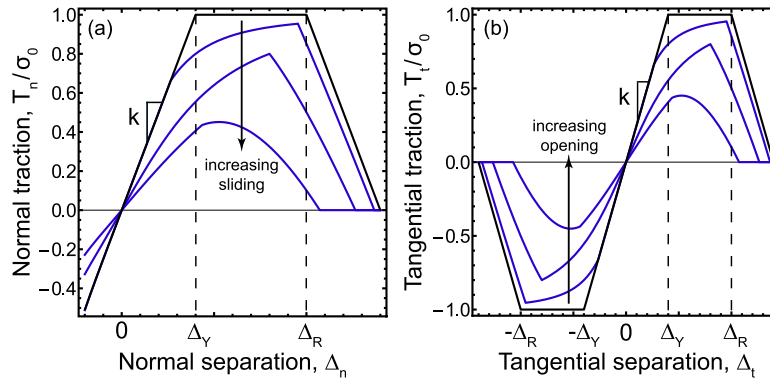


Fig. 2. Schematic of piecewise cohesive law used in analysis for normal (a) and tangential (b) tractions.

3.1. Material description, geometry and loading

Here, we implement a piecewise cohesive law identical to that used in the work of Pro et al. (2015a,b) and Lim et al. (2016), and similar in spirit to that of Strom and Parmigiani (2014). The cohesive law is shown graphically in Fig. 2, and is completely defined by three parameters: a cohesive stiffness (k), the peak strength (σ), and work of separation (Γ). As illustrated in Fig. 2, the normal and tangential behaviors are coupled, such that normal separation will alter the tangential tractions that can be maintained, and vice versa. The full mathematical description of the cohesive law is given in Pro et al. (2015a), and is omitted here for brevity. Since different cohesive laws are prescribed for elements along the material interface, than those in the bulk, we adopt the notation of $(k_i, \sigma_i, \Gamma_i)$ for the cohesive elements along the material interface, and $(k_b, \sigma_b, \Gamma_b)$ for the cohesive elements in the bulk (between adjacent elements). The implications of these parameters and their relative values are discussed in detail in the next section. The chosen cohesive law dictates that the cohesive work of separation Γ is independent of the specific loading path to full rupture (Lim et al., 2016). As such, the associated material toughness is independent of the mode mix, an assumption typically employed with brittle materials. It is worth noting that the form of the cohesive law is easily modified to account for mode-dependent toughness, by specifying different values for the cohesive work of normal separation and the cohesive work of tangential separation (Xu and Needleman, 1994).

The geometry considered in this work consists of a semi-infinite interface crack subjected to mixed-mode loading, as shown schematically in Fig. 3a. The disk is assumed to have homogeneous elastic moduli and Poisson's ratio, denoted as E_b and ν_b , as shown in Fig. 3b. Plane strain conditions were enforced in all calculations. The disk is loaded by applying displacements along the outer radius (R_o) that are defined by the asymptotic elastic crack tip fields for an interface crack (Tada et al., 1973). These displacements are increased monotonically by increasing the associated energy release rate for the parent interface crack, G_i . A given case is completely defined by prescribing $G_i(t)$ (where time is arbitrary), the mode mix through the phase angle ψ (fixed in time), and the bulk elastic constants E_b and ν_b . The phase angle defining the mode mix can be found via the equation

$$\psi = \tan^{-1} \left(\frac{K_{II}}{K_I} \right) \quad (2)$$

Using this relation, the stress intensity factors can be expressed in terms of the phase angle and energy release rate for the interface crack as follows:

$$K_I = \cos \psi \sqrt{\bar{E}_b G_i}; \quad K_{II} = \sin \psi \sqrt{\bar{E}_b G_i} \quad (3)$$

where $\bar{E}_b = E_b / (1 - \nu_b^2)$. Using these relationships, the displacements (for an isotropic material) take the form:

$$u_i(r, \theta) = K_I \sqrt{r} f_i^I(r, \theta, E_b, \nu_b) + K_{II} \sqrt{r} f_i^{II}(r, \theta, E_b, \nu_b) \quad (4)$$

where f_i^I and f_i^{II} are dimensionless functions and can be superposed with prescribed values of K_I and K_{II} to span the full range of mode mixity, similar to the approach of Zavattieri et al. (2008). As these functions are cumbersome to express in their complete mathematical form, the reader is referred elsewhere for the details (Tada et al., 1973).

In all calculations, the disk was ramp loaded in displacement control past the point where the parent crack begins to advance. For all subsequent analysis, crack advance is defined as the point at which the interface separation between the elements directly ahead of the crack tip exceeds the full rupture separation ($\Delta_R + \Delta_Y$) at either Gaussian integration point. The critical macroscopic ERR of the parent crack at initiation is denoted as G_i^c . Provided that kinking is avoided, the process zone is sufficiently resolved, and the specimen is large enough that the far field elastic stresses are the dominant driving force (i.e., small scale yielding), then the value of G_i^c is equal to the cohesive work of separation.

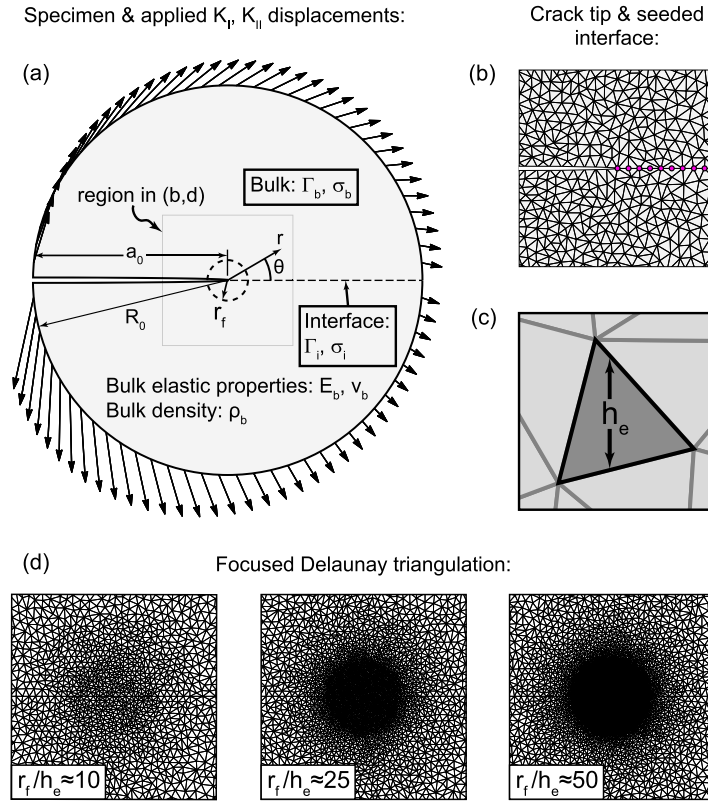


Fig. 3. Schematic of (a) simulated disk with Mode I/II displacements applied along the outer boundary (b) crack tip and seeded interface (c) characteristic element size h_e and (d) focused Delaunay triangulation with varying mesh densities within focused region ($r < r_f$), where r is the radial coordinate in a polar coordinate system centered at the crack tip.

The authors have also performed calculations indicating the case where elastic mismatch is present in the disk with non-zero Dundurs’ parameters (both $\alpha \neq 0$ and $\beta \neq 0$) which showed preliminary agreement with the corresponding He and Hutchinson results. However, due to the complications of the oscillating stress field ahead of the crack tip, these results are not shown here as they required additional verification within the context of the cohesive zone model.

3.2. Controlling length-scales and numerical considerations

The presence of the cohesive zones introduces several new length scales into the problem not present in conventional finite element analysis. First and foremost, the elastic stiffness of the material as a whole is altered via the cohesive stiffness, as noted by Turon et al. (2007). It can be shown that for a regular grid of finite elements connected by elastic cohesive elements, the effective (composite) modulus E_c can be expressed in the following form:

$$\frac{E_c}{E} = \frac{k_0 h_e}{k_0 h_e + E(1 + c_0)} \tag{5}$$

where c_0 is a constant that depends on the aspect ratio of the elements, and E is the modulus used in the conventional element description, k_0 is the stiffness of the cohesive law, and h_e is the element size. The modulus ratio E_c/E approaches unity in the limit of infinitely stiff interfaces (i.e., $h_e k_0 \gg E$). For all practical purposes, a large value of the cohesive stiffness k_0 may be implemented to achieve a modulus ratio near unity for any given element size.

Note that increasing the value of $h_e k_0/E$ also decreases the requirement on time stepping for numerical stability. One can show that the time step for numerical stability scales inversely with the square root of the dimensionless cohesive stiffness, indicating a tradeoff between simulation cost and accuracy of the material modulus. Turon et al. suggested a dimensionless cohesive stiffness of $h_e k_0/E = 50$ (Turon et al., 2007), which will be used for all subsequent calculations and produces near identical results to continuum FEA simulations, while keeping the simulation cost reasonable. Note that if multiple moduli are present, then the element modulus E should be taken as the largest modulus in the problem.

The presence of the cohesive zones also introduces a fracture length scale into the problem, ℓ_{cz} , which has been shown to scale as follows (Parmigiani and Thouless, 2006):

$$\ell_{cz} = M \frac{E\Gamma}{\sigma^2} \tag{6}$$

where Γ is the work of separation of the cohesive interface, and σ is the peak strength of the cohesive law. The constant M depends on the specific model of the cohesive law, which has been proposed to take on values ranging from 0.21 to 1 by various authors (Barenblatt, 1959; Dugdale, 1960; Falk et al., 2001; Hillerborg et al., 1976; Hui et al., 2003; Irwin, 1997; Rice, 1979); here we use a value of $M = 1$ for simplicity. The length scale ℓ_{cz} can be thought of as the size of the fracture process zone; it must be small compared to any linear dimension of the specimen (e.g., $\ell_{cz} \ll R_0$) in order for linear elastic fracture mechanics to apply (i.e. G controlled crack stability), but large compared to the characteristic mesh size (h_e) in the vicinity of the crack tip to resolve the non-linear behavior in this region. However, as noted by Turon et al. (2007), the specific mesh resolution within the fracture length required for numerical accuracy is not generally agreed upon (Carpinteri et al., 2003; Dávila et al., 2001; Falk et al., 2001; Moës and Belytschko, 2002), and for all practical purposes is problem-specific. By Eq. (6), one can alter the mesh resolution for a given material (or interface) by artificially increasing the size of the fracture process zone (e.g. by reducing the cohesive strength σ with a concomitant change in critical separation Δ_R such that the toughness is held fixed). It is critically important to note that when the interface and bulk materials have different work-of-separation and strengths, there are multiple cohesive length scales, reflecting the difference in fracture process zones along the interface and the bulk. In such instances, additional impacts of changes to cohesive parameters must be considered; this is discussed in detail in the dimensional analysis of Section 3.3.

An automatic Delaunay triangulation algorithm is used to generate the mesh for a disk of radius R_0 , as shown in Fig. 3. The meshing algorithms from the open-source C code *Triangle* are used in this work (Shewchuk, 1996; 2002). The elements are focused at the center of the disk for computational efficiency, as shown in Fig. 3d, with varying mesh densities. The focused region of concentrated elements is contained within a circle of radius r_f , as shown in Fig. 3. For convenience, the characteristic element size is defined as the average effective triangle height h_e within the focused region (shown in Fig. 3c), and can be expressed as follows:

$$h_e = \sqrt{\frac{\pi r_f^2}{N_{e,f}}} \quad (7)$$

where $N_{e,f}$ is the number of elements in the focused region. Ordinary constant strain 3-noded triangular finite elements are used for simplicity, with each element coupled to the adjacent element through the cohesive law described previously.

Note that the non-linearity present in the cohesive law leads to a set of highly non-linear governing equations, which can be prone to convergence difficulties when solving the quasi-static case, particularly at the onset of cohesive rupture. For this reason, the full dynamic equations of motion are solved (e.g., with inertial terms) using an in-house developed explicit time stepping code (very much similar to the approach of Xu and Needleman, 1994²). However, *quasi-static loading conditions were enforced* throughout the simulations. This was done by applying the displacement boundary conditions very slowly, such that the results did not change upon *decreasing the loading rate*. Note that this is a general approach in which the computing time *does not depend* on the non-linearity in the cohesive law, and has been used by other authors for complicated non-linear problems (Aoyanagi and Okumura, 2009).

Both stiffness and mass damping were introduced into the calculations (as described in Cook et al., 2007). The dimensionless damping ratio was set at $\zeta = 0.5$ so that the system was near critical damping levels, which allows for larger load rates to be applied. Here, the damping ratio is defined through the material properties as follows:

$$\zeta = \frac{1}{2} \left(\frac{2R_0 c_M}{\pi} \sqrt{\frac{\rho_b}{E_b}} + \frac{c_K \pi}{2R_0} \sqrt{\frac{E_b}{\rho_b}} \right) \quad (8)$$

where c_M and c_K are the mass and stiffness damping coefficients, respectively.

The time stepping algorithm was implemented in C++. The data structure was designed for enhanced spatial and temporal CPU cache locality, which reduces the amount of memory access and improves performance. It was parallelized using PThreads with low overhead synchronization primitives. A Linux shell (.sh) script was used for generating various meshes and loading conditions, associated with sweeping through dimensionless variables in the parameter space.

3.3. Dimensionless analysis and parametric studies

The critical value of the applied (far field) energy release rate G_i^* of the parent crack that leads to crack growth depends on a large number of material properties: the cohesive parameters (Γ_i , Γ_b , σ_i , σ_b , k_i , k_b), the plane strain modulus \bar{E}_b , the mesh size h_e , and the disk radius R_0 . Presented in dimensionless form, this dependency can be expressed as:

$$\frac{\Gamma_{b,i}}{G_i^*} = f \left(\psi_f, \frac{h_e k_i}{E_b}, \frac{h_e k_b}{E_b}, \frac{E_b \Gamma_b}{\sigma_b^2 h_e}, \frac{\Gamma_i \sigma_b^2}{\Gamma_b \sigma_i^2}, \frac{E_b \Gamma_b}{\sigma_b^2 R_0}, \frac{E_b \Gamma_i}{\sigma_i^2 R_0}, \frac{\Gamma_b}{\Gamma_i}, \frac{\sigma_i}{E_b}, \frac{\sigma_b}{E_b}, \frac{\Gamma_i}{E_b R_0}, \frac{\Gamma_b}{E_b R_0} \right) \quad (9)$$

These dimensionless groups agree with those of Strom and Parmigiani (2014), with a few minor changes. When changing the dimensionless bulk-to-interface work of separation ratio Γ_b/Γ_i , and holding process zone resolution constant, the

² Xu and Needleman (1994) developed a general method that accounts for arbitrarily large elemental strains and rotations. Here, we assume small rotations and small strains.

bulk-to-interface work of separation ratio cannot be changed *without also altering the cohesive bulk-to-interface strength ratio*; therefore these two parameters cannot be changed independently. For this reason, we have replaced σ_i/σ_b in the dimensionless analysis with:

$$\frac{\ell_{cz}^i}{\ell_{cz}^b} = \frac{\Gamma_i \sigma_b^2}{\Gamma_b \sigma_i^2} \quad (10)$$

which is permitted by dimensionless analysis so long as the bulk-to-interface work of separation ratio Γ_b/Γ_i is still included in the analysis as reference. This is advantageous in the current formulation because the work of separation ratio Γ_b/Γ_i may be changed independently while maintaining a constant mesh resolution with respect to the fracture process zones. Using these dimensionless parameters provides a straightforward means to modulate cohesive parameters while ensuring small-scale yielding and a fixed resolution in the fracture process zones.

As pointed out in [Strom and Parmigiani \(2014\)](#), the ratios of the cohesive shear to normal strength of the interface or bulk also play a role in the analysis. However, here we assume an ideally brittle material, such that the ratio of the normal to tangential cohesive work of separation is set to unity ([Begley and Hutchinson, 2016](#)), along with the cohesive normal and shear strengths (for both the interface and the bulk). Therefore these parameters have been omitted from the dimensionless analysis.

[Eq. \(11\)](#) represents a large parameter space that is quite challenging and computationally expensive to map out in its entirety. However, by ensuring that the specimen dimensions are much larger than the fracture length, [Eq. \(11\)](#) can be reduced to eliminate any terms that depend on the disk radius, R_0 . This was done by trial and error such that the simulation results did not change upon switching to a larger disk. The radius was chosen such that both the interface and bulk fracture lengths were less than a critical value, e.g., $\frac{\ell_{cz}^i}{R_0} < \eta$ and $\frac{\ell_{cz}^b}{R_0} < \eta$. A value of $\eta \approx 0.035$ was chosen such that the critical ERR of the parent crack was left unchanged upon switching to a larger disk radius R_0 in pure mode I loading. The dimensionless interface stiffness terms $h_e k_{i,b}/E_b$ may also be omitted, via the reasoning in [Section 3.2](#).

The number of relevant dimensionless terms in the analysis is therefore significantly reduced:

$$\frac{\Gamma_{b,i}}{G_i^*} = f\left(\psi, \frac{E_b \Gamma_b}{\sigma_b^2 h_e}, \frac{\Gamma_i \sigma_b^2}{\Gamma_b \sigma_i^2}, \frac{\Gamma_b}{\Gamma_i}, \frac{\sigma_i}{E_b}, \frac{\sigma_b}{E_b}\right) \quad (11)$$

This presents a straightforward path for an efficient parameter study, as follows. First, we fix bulk-to-interface work of separation ratio Γ_b/Γ_i and the interface-to-bulk fracture length ratio $\ell_{cs}^i/\ell_{cz}^b = \frac{\Gamma_i \sigma_b^2}{\Gamma_b \sigma_i^2}$ at unity, and vary phase angle over different bulk mesh resolutions $\ell_{cz}^b/h_e = \frac{E_b \Gamma_b}{\sigma_b^2 h_e}$ until consistent results are obtained. For these calculations, we initially chose $\frac{\sigma_b}{E_b} = \frac{\sigma_i}{E_b} = 0.0087$ and held it fixed. Note that the cohesive strength is analogous to the atomic bond rupture strength for a brittle material, and realistic values of $\frac{\sigma_0}{E_b}$ would be much larger (≈ 0.044 assuming $\sigma_0 = 10$ GPa, $E = 200$ GPa, and $\nu = 0.35$). However, increasing the cohesive strength (while maintaining the bulk fracture length resolution) has substantial implications with regard to the computational cost.

With the mesh resolution established, we then back-checked the effect of the dimensionless cohesive strength $\frac{\sigma_{i,b}}{E_b}$ with a separate parameter study that completely isolated it completely against all other variables. This parameter study was performed by fixing ψ , $\frac{E_b \Gamma_b}{\sigma_b^2 h_e}$, $\frac{\Gamma_b}{\Gamma_i}$, and $\frac{\Gamma_i \sigma_b^2}{\Gamma_b \sigma_i^2}$, and varying $\frac{\sigma_{b,i}}{E_b}$ over the range 0.002 to 0.014 (values greater than 0.014 were avoided as they yielded calculation times over 10 days). The same study was repeated for each value of $\frac{E_b \Gamma_b}{\sigma_b^2 h_e}$ that was used in any other simulation. As will be shown, this study revealed that the ratios $\sigma_{i,b}/E_b$ had a second order effect on the results; therefore the following approximation was assumed to hold for the remainder of the calculations:

$$\frac{\Gamma_{b,i}}{G_i^*} \approx f\left(\psi, \frac{E_b \Gamma_b}{\sigma_b^2 h_e}, \frac{\Gamma_i \sigma_b^2}{\Gamma_b \sigma_i^2}, \frac{\Gamma_b}{\Gamma_i}\right) \quad (12)$$

Finally, a very large parameter study was performed to examine the effect of both the interface-to-bulk fracture length ratio and the bulk-to-interface work of separation ratio ($\frac{\Gamma_i \sigma_b^2}{\Gamma_b \sigma_i^2}$ and $\frac{\Gamma_b}{\Gamma_i}$, respectively) at fixed $\frac{E_b \Gamma_b}{\sigma_b^2 h_e}$. For these calculations, about 10 different phase angles and 10 different bulk-to-interface toughness ratios were each run at 3 different levels of $\frac{\Gamma_i \sigma_b^2}{\Gamma_b \sigma_i^2}$, for a total of about 300 simulations. In these calculations, each simulation had a wall time of about 2 days using 8 cores each. About 30 jobs were run simultaneously, for a total of about 3 weeks of straight computation time. The UCSB supercomputers KNOT and IRP were utilized in all cases to facilitate the computations.

4. Results and discussion

4.1. Kink nucleation for $\Gamma_i = \Gamma_b$ and $\sigma_i = \sigma_b$: Effect of mesh resolution

In this section, we illustrate the efficacy of the framework by considering the simplest case of a mixed mode interface crack with isotropic toughness, i.e. identical bulk and interface toughness ratios. The interface and bulk strengths are also

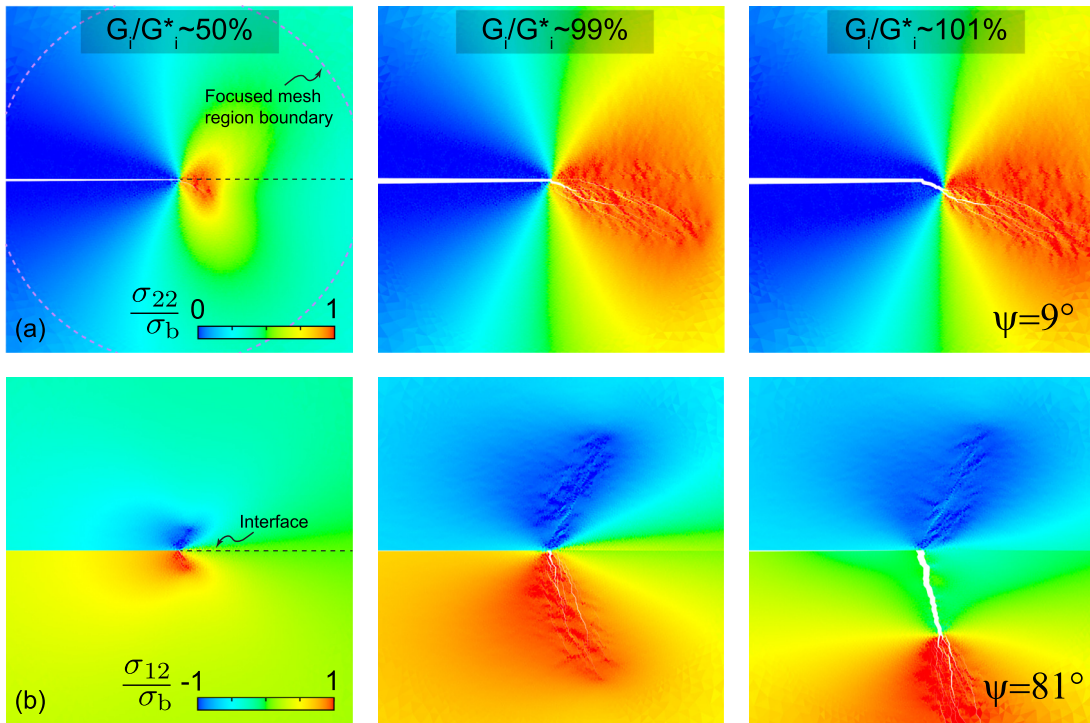


Fig. 4. Stress contours at various loading increments in the simulation for two levels of mode mix,(a) $\psi = 9^\circ$ and (b) $\psi = 81^\circ$. For all cases, the mesh resolution parameter is $\ell_{cz}^b/h_e = \frac{E_b\Gamma_b}{\sigma_b^2 h_e} = 178$, $\sigma_i = \sigma_b$ and $\Gamma_i = \Gamma_b$ (such that $\ell_{cz}^i/\ell_{cz}^i = 1$).

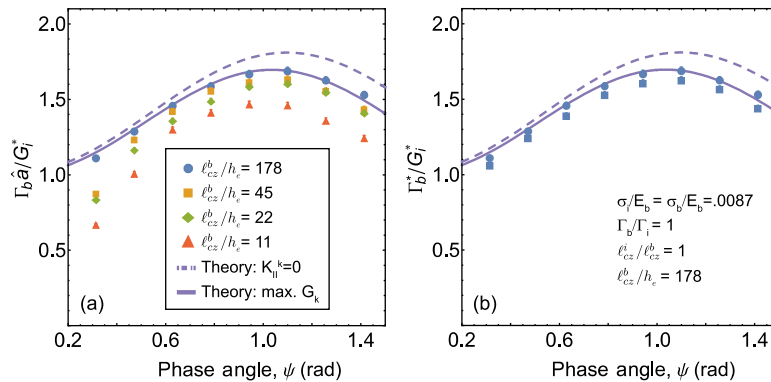


Fig. 5. Critical energy release rate of parent crack as a function of applied phase angle ψ and process zone resolution $\ell_{cz}^b/h_e = \frac{E_b\Gamma_b}{\sigma_b^2 h_e}$. Results shown for $\Gamma_b = \Gamma_i$ and $\sigma_b = \sigma_i$, such that the cohesive lengths scales of the interface and bulk are identical. The inverse of G_i^*/Γ_b is used to match the presentation of He and Hutchinson (1989b).

assumed to be identical, $\sigma_i = \sigma_b$, such that the process zones along the interface and throughout the bulk are the same size. Stress contours resulting from the simulations are shown in Fig. 4 for various loading increments. In all plots, the stresses are normalized by the bulk cohesive strength $\sigma_b = \sigma_i$. The direction of the emergent crack from the fracture process zone depends strongly the mode mix, as expected, with strong mode II loading leading to high angle kinks.

This situation is identical to that of He and Hutchinson (1989b), with the important exception that a putative kink crack is not included in the present analysis. Hence, this simulation effectively determines if the behavior of crack nucleation is comparable to the growth criteria associated with the presence of a flaw that is much larger than the process zone. The two key outcomes of the simulation are the critical value of the far field energy release rate G_i^* , as a function of mode mix (shown in Fig. 5), and the direction of crack growth, defined by kink angle, $\tilde{\Omega}$ (shown in Fig. 6). Results are shown for several different meshes; the normalized parameter in the inset is essentially the number of elements in the estimated process zone.

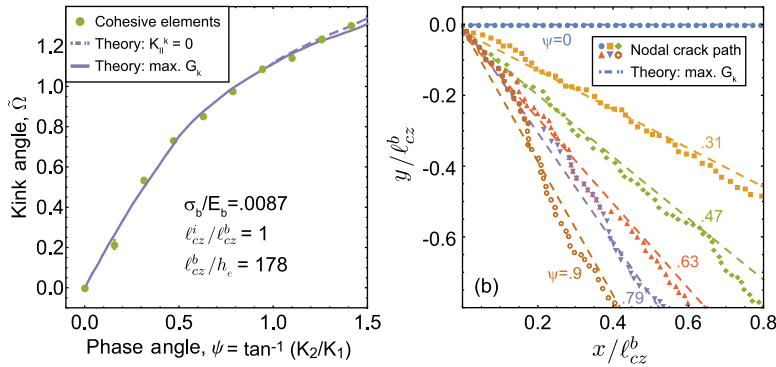


Fig. 6. (a) Kink angle measured through regression analysis as a function of applied phase angle ψ for a completely isotropic system, i.e. $\sigma_i = \sigma_b$, and $\Gamma_i = \Gamma_b$. The solid line is the prediction of He and Hutchinson (1989b,c) assuming $G_k^{max} = \Gamma_b$, while the dashed line is the He and Hutchinson (1989b,c) result assuming $K_{II} = 0$ at the tip of the kink crack. The critical energy release rate for growth in this system is shown in Fig. 5a. The data points used to compute the average kink angle are shown directly in (b), where the crack path is defined as a traction free surface where the opening displacement exceeds the full rupture displacement $\Delta_R + \Delta_Y$.

It has been demonstrated by several authors that three basic criteria are suitable for capturing the kinking plane: the maximum ERR criteria, the zero mode-II criteria, and the maximum principal stress criteria (Cotterell and Rice, 1980; He and Hutchinson, 1989b; Hutchinson and Suo, 1992). It is generally agreed that there is little practical distinction between the first two criteria (He and Hutchinson, 1989b), and in most loading configurations the last two criteria are identical (although one could envisage cases where maximum principal stress criteria is different from the $K_{II}=0$ criteria in the presence of substantial in-plane stress, where the $K_{II}=0$ criteria corresponds to the minimum principal stress). Therefore, for subsequent results, both the $K_{II}=0$ and maximum ERR criteria are shown from the predictions of He and Hutchinson (1989b,c).

One can immediately see from Figs. 5 and 6 that, with sufficient mesh resolution, the present framework produces the results of He and Hutchinson (1989b,c). This clearly indicates that the kink nucleation problem, when $\Gamma_i = \Gamma_b$ and $\sigma_i = \sigma_b$, gives near identical results to the case with a putative flaw according to the criterion $G_k = \Gamma_b$. In all cases shown in Fig. 5, the coarse meshes overestimate the critical far-field load, G_i^* (or underestimate its reciprocal $1/G_i^*$), and in that sense cannot be regarded as conservative.

For the results shown in Fig. 5a, the bulk work of separation Γ_b was normalized by the mesh tortuosity \hat{a} , defined as the ratio of actual crack length (accounting for the jaggedness of the mesh edge faces) to the length of a straight line joining the initial and final crack tip at a distance equal to the fracture process zone length. Fig. 5b shows the effect of this normalization; the same results are plotted for fixed process zone resolution, only now with both the normalized ($\Gamma_b \hat{a}$) and unnormalized work of separation (Γ_b). It is hypothesized that artificial tortuosity introduced by random Delaunay triangulation slightly increases the macroscopic toughness due to the additional surface area traversed by a crack relative to the area of a straight path. For most calculations this was about 5%; the results are in excellent agreement with those of He and Hutchinson (1989b,c) when accounting for the effect of tortuosity.

The averaged kink angle of the emergent crack (Fig. 6) was computed as the inverse tangent of the slope of the line of best fit through all the cracked nodes over one bulk fracture length. The positions of initially coincident nodes along the crack faces were averaged along the crack path and used for the regression analysis. As shown in Fig. 6, the results are again in excellent agreement with the predictions of He and Hutchinson (1989b).

Regarding the effect of mesh resolution shown in Fig. 5, similar insights have been drawn with cohesive zone models previously for cracks growing along pre-defined paths (Carpinteri et al., 2003; Dávila et al., 2001; Falk et al., 2001; Moës and Belytschko, 2002), hence it appears that this concept may be generalized for arbitrary crack trajectories within a random mesh as well (when accounting for the mesh tortuosity \hat{a}). As the number of nodes within the bulk fracture length is increased, the number of potential paths from one node to another increases, hereby increasing the number of averaged kink angles that may accurately be resolved. Additionally, the distribution in mesh tortuosity is narrowed as the nodal sample size is increased, leading to more consistent values of \hat{a} .

It is worth noting that the authors performed numerical experiments with other mesh structures as well, including a radial fan mesh as well as a mesh of cross triangulated quadrilaterals (exactly as in Xu and Needleman, 1994). However, consistent results were unable to be obtained with non-random meshes. The radial fan mesh required triangles of very high aspect ratio focused at the crack tip, when accounting for the angular resolution in kinking required ($\approx 1 - 2^\circ$). While this mesh produces a theoretical initial mesh tortuosity of zero during the initial stages of crack advance, none of the attempted calculations were numerically stable for the range of time steps that would keep the simulation cost reasonable; therefore these calculations have been omitted from the results section.

Finally, all of the calculations shown in Figs. 4–6 hold the dimensionless cohesive strengths constant, i.e. $\sigma_{b,i}/E_b = 0.0087$. Put another way, the conditions driving growth of the pre-crack were initially assumed to be energetic, with fracture controlled by $G = \Gamma_b = \Gamma_i$. As mentioned, a set of calculations was performed to confirm this assumption; the dimensionless

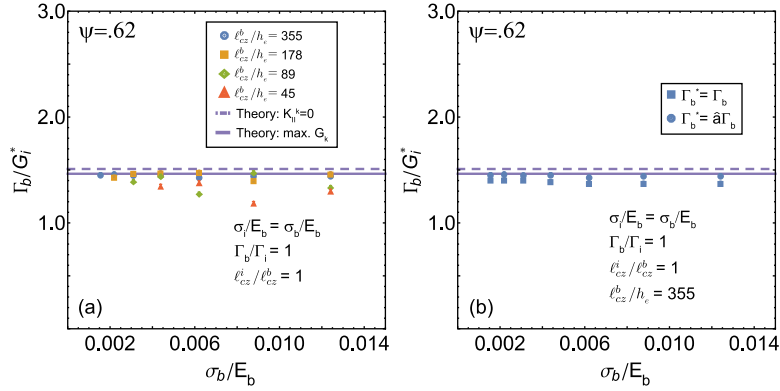


Fig. 7. (a) Relative critical ERR of parent crack as a function of dimensionless interface strength for various bulk fracture length resolutions and (b) relative critical ERR of interface (both normalized and unnormalized) as a function of dimensionless interface strength (for fixed bulk fracture length resolutions).

parameters ψ , ℓ_{cz}^b/h_e , ℓ_{cz}^i/ℓ_{cz}^b , and Γ_b/Γ_i were fixed, while σ_b/E_b was varied. Note that this will inevitably increase the fracture length relative to the disk radius R_0 . Therefore, whenever the cohesive strength input was changed, the disk radius was also changed in order to keep all of the radius dependent terms in Eq. (11) constant. The load rate and damping parameters were also adjusted such that the dimensionless loading rate and damping ratio (respectively) remained constant. Fig. 7a indicates that at sufficiently high resolution, the energetic condition for failure is recovered, as indicated by the nearly perfect constant data for $\ell_{cz}^b/h_e = 178$ and above. Fig. 7b shows only the case with the highest resolution; the critical kinking energy release rate is clearly independent of the bulk and interface cohesive strength. Fig. 7 also shows the effect of the tortuosity correction, which again brings the results in near excellent agreement with that of He and Hutchinson (1989b). However, Fig. 7a indicates that at lower resolution this outcome may not be guaranteed, as suggested by the somewhat oscillatory data for $\ell_{cz}^b/h_e < 178$.

4.2. Impact of different bulk and interface process zone sizes

In the previous section, the ratio of process zone lengths for the interface and bulk, defined by $\ell_{cz}^i/\ell_{cz}^b = \Gamma_i\sigma_b^2/(\Gamma_b\sigma_i^2)$, was held constant at unity while $\Gamma_b = \Gamma_i$. A more interesting study involves the transition between kinking and interface failure, which is controlled by interacting process zones (for the interface and bulk) that have different length-scales. To address this, a large parameter study was also performed by independently altering each of the phase angle (ψ), the process zone size ratio $\ell_{cz}^i/\ell_{cz}^b = \Gamma_i\sigma_b^2/(\Gamma_b\sigma_i^2)$, and the work of separation ratio Γ_b/Γ_i .

The results in Fig. 8a show a map of kinking and interface delamination as a function of both phase angle ψ and the work of separation ratio Γ_b/Γ_i , for the case where $\ell_{cz}^i = \ell_{cz}^b$. This figure was constructed by brute force, i.e. running simulations with the parameter combinations shown and tabulating whether the crack advanced along the interface or kinked into the bulk. The solid line corresponds to the theoretical bulk interface toughness that would be required to suppress kinking according to the He and Hutchinson (1989b,c) criterion; beneath this line, Γ_b is not high enough to suppress kinking. For this case, in which $\ell_{cz}^i = \ell_{cz}^b$, the results shown in Fig. 8a illustrate that a significantly higher bulk toughness is required to suppress nucleation of a kink crack. The discrepancy clearly increases with increasing mode mix; we postulate that the process zone along the interface reduces the constraint of the interface against the emergence of a high angle kink. While similar to Fig. 5a, it should be noted that Fig. 8a does not indicate the value of the far-field energy release rate required to drive kinking- this is shown in Fig. 9.

Fig. 8b provides an alternative representation of the kink/delamination map for $\ell_{cz}^i = \ell_{cz}^b$, based on the same He and Hutchinson (1989b,c) criterion for kinking. The criterion can be stated as follows: kinking occurs when

$$\frac{G_k}{\Gamma_b} > \frac{G_i}{\Gamma_k} \quad \text{or} \quad \tilde{\Gamma}_R \equiv \frac{G_i\Gamma_b}{G_k\Gamma_i} < 1 \quad (13)$$

where G_k is the energy release rate for a putative kink in the direction that maximizes its value, while G_i is the energy release rate of the parent crack (both compiled by He and Hutchinson, 1989b; He and Hutchinson, 1989c). One may interpret $\tilde{\Gamma}_R$ as the ratio of the bulk toughness to that of the interface, but normalized by the ratio required to suppress kinking according to putative kink calculations. From Fig. 8b, it is clear that for $\ell_{cz}^b = \ell_{cz}^i$ kinking can occur even when $G_k/\Gamma_b < G_i/\Gamma_i$, i.e. $\tilde{\Gamma}_R > 1$. In essence, the interacting process zones at the interface and in the bulk lower the value of Γ_i needed to suppress delamination and favor kink nucleation.

Fig. 8c and d show the boundaries between delamination and kinking for cases where $\ell_{cz}^i \neq \ell_{cz}^b$. It is clear that the He and Hutchinson (1989b,c) criterion for kink stability best matches nucleation conditions when the process zone on the interface is slightly larger than that in the bulk, i.e. $\ell_{cz}^i \sim 1.5\ell_{cz}^b$. At low phase angles, the bulk toughness required to suppress kinking is lower than He and Hutchinson (1989b,c) suggest, while at higher phase angles the bulk toughness required to suppress

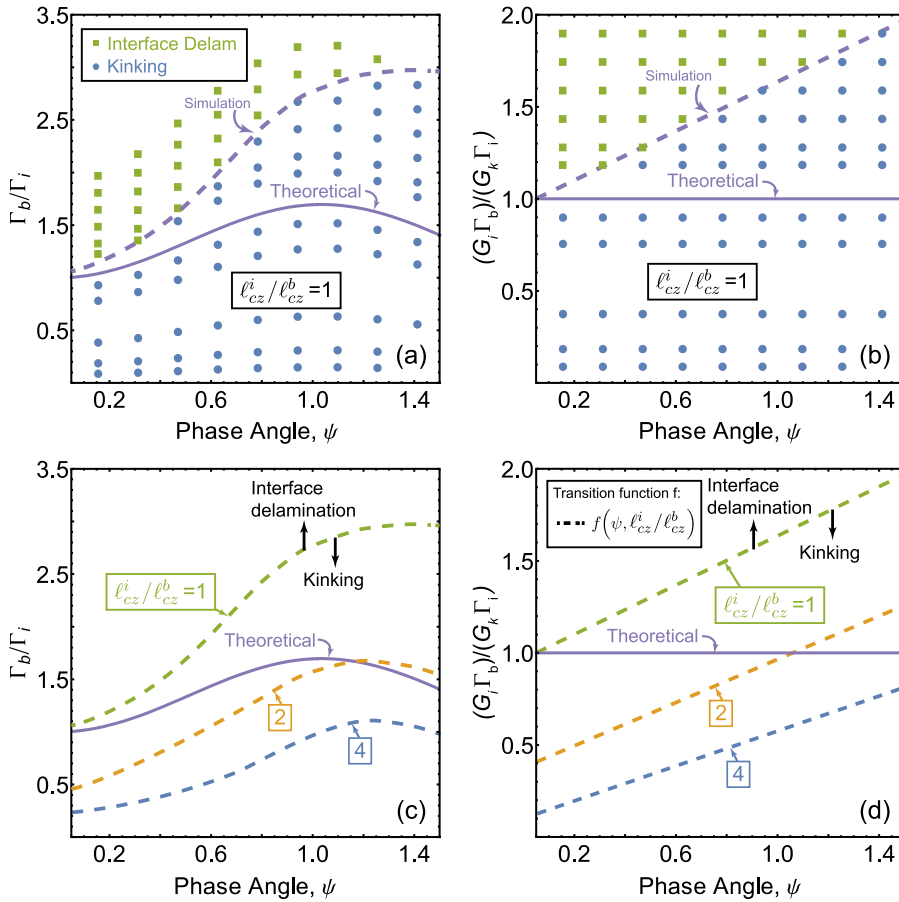


Fig. 8. Transition between kinking and interface fracture as a function of (a) phase angle and work of separation ratio with all data points shown, (b) phase angle and the normalized work of separation ratio equivalent to the He and Hutchinson (1989b,c) kinking criteria, (c) phase angle and work of separation ratio for several process zone ratios (d) phase angle and the normalized work of separation ratio equivalent to the He and Hutchinson (1989b,c) kinking criteria. The dashed lines in (d) represent the critical values of the He and Hutchinson (1989b,c) criterion from the cohesive zone model (CZM) simulations for fixed process zone size ratios. For all calculations shown in (a)–(d) the bulk fracture length resolution was set at $\ell_{cz}^b/h_e = 178$.

kinking is higher. Clearly, a large interface process zone (in comparison to the bulk process zone) strongly suppresses kinking in favor of interface delamination. This is entirely expected and is supported by experiments on glass-epoxy systems involve much larger process zones associated with yielding in the epoxy (Liechti and Chai, 1991).

Simply put, kink nucleation is more likely than the He–Hutchinson criterion suggests when the fracture process zones interact and are approximately equal. Conversely, when the interface fracture process zone is much larger than the bulk fracture process zone, kink nucleation is much less likely than suggested by the He–Hutchinson stability criterion. This disagreement is a trend also realized by Strom and Parmigiani (2014) and Parmigiani and Thouless (2006), who tested the deflection versus penetration criteria with cohesive laws (rather than the kinking versus delamination as in the present work). More specifically, the transition between kink nucleation and delamination is dependent on both the phase angle and the normalized toughness ratio $\tilde{\Gamma}_R$. Thus, the kink nucleation criterion can be expressed as:

$$\tilde{\Gamma}_R < f\left(\psi, \frac{\ell_{cz}^i}{\ell_{cz}^b}\right) \tag{14}$$

where f is a linear function in ψ and non-linear with respect to the ratio of the process zone sizes.

Fig. 9 shows the critical energy release rate of the parent crack that drives failure, G_i^* , normalized by the toughness that controls failure, Γ^* . That is, when kinking occurs, $\Gamma^* = \Gamma_b$, while when delamination occurs, $\Gamma^* = \Gamma_i$. Data is shown in Fig. 9 for cases with $\ell_{cz}^i = \ell_{cz}^b$, $\ell_{cz}^i = 2\ell_{cz}^b$ and $\ell_{cz}^i = 4\ell_{cz}^b$, respectively. Further, data was generated for constant normalized toughness ratios, $\tilde{\Gamma}_R$. The fracture path is indicated by circles for kink nucleation, and squares for delamination.

Consider Fig. 9a for an isotropic material with $\ell_{cz}^i = \ell_{cz}^b$: for most cases, the fracture modality is fixed across all values of mode mix for a given value of $\tilde{\Gamma}_R$; for others, such as $\tilde{\Gamma}_R = 1.35$, the modality is delamination at low mode mix but switches to kinking at higher values of mode mix. This switch in modality does not happen when $\tilde{\Gamma}_R \ll 1$ (kinking almost always favored), and when $\tilde{\Gamma}_R \gg 1$ (delamination is almost always favored). As indicated by Fig. 9a, when $\ell_{cz}^i = \ell_{cz}^b$ and

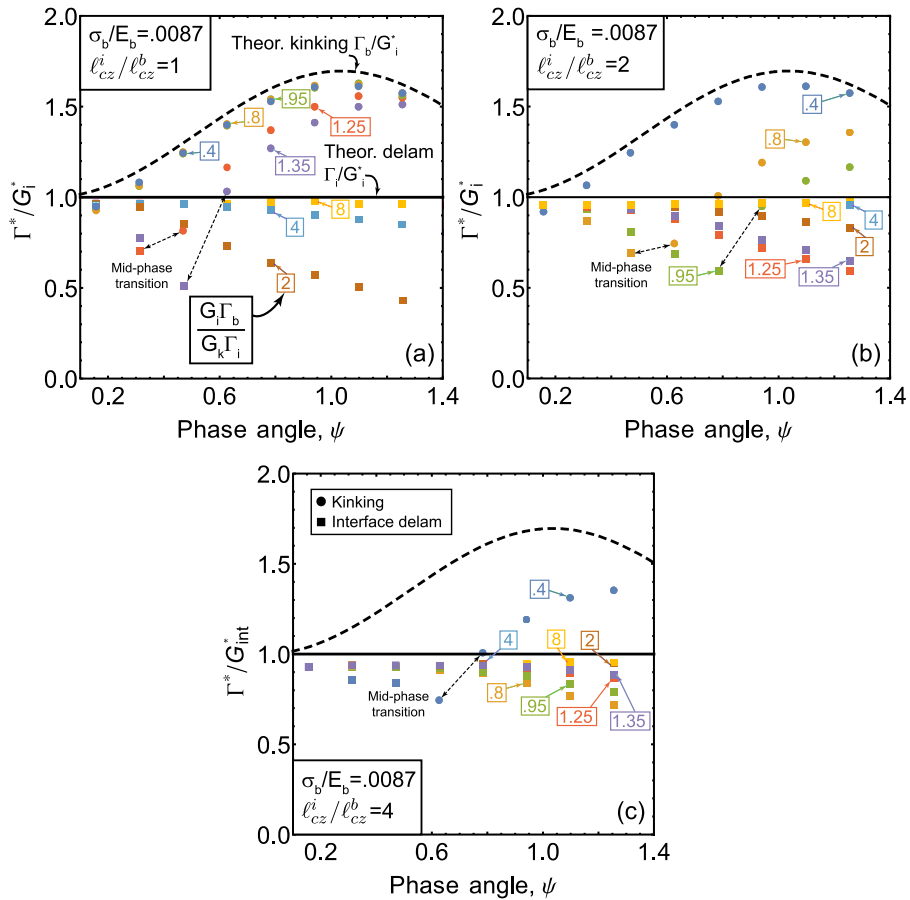


Fig. 9. Relative critical initiation ERR for various interface-to-bulk fracture length ratios as a function of applied phase angle ψ and normalized toughness ratio $\tilde{\Gamma}_R$.

$\tilde{\Gamma}_R \sim 1$, the critical far-field energy release rate required to trigger kink nucleation is virtually identical to that required to drive a putative kink crack. However, as the normalized toughness $\tilde{\Gamma}_R$ increases closer to the transition to delamination, the critical G_i to nucleate a kink crack is higher than that required to drive a putative crack. This is because the fracture process zone at the interface provides additional dissipation that must be overcome to nucleate the kink.

Similarly, Fig. 9a demonstrates that one recovers the interface cracking condition $G_i = \Gamma_i$ when the normalized toughness ratio is very large, i.e. a bulk toughness that is much larger than that required to suppress kinking. However, when the normalized toughness ratio is moderate and close to the transition, e.g. $\tilde{\Gamma}_R = 2$, the critical G_i required to drive interface cracking is higher than Γ_i . This is because the fracture process zone for kink nucleation is present and provides additional dissipation that must be overcome to drive interface cracking. For these cases, the process zone for kinking never reaches a critical value, such that a kink does not nucleate. The upper limit for the additional interface dissipation in the bulk is simply the bulk work of separation ratio Γ_b ; therefore the upper limit in the apparent toughness of the interface is simply $\Gamma_b + \Gamma_i$. It was confirmed in all simulations that this value was not exceeded.

Note that in many brittle systems where interfacial failure occurs, there would be virtually no contribution to the interface toughness due to energy dissipation in the adjoining bulk material. Conversely, in cases where kinking in the bulk occurs in a brittle system, one would expect no contribution from the interface to the bulk toughness. This could be accounted for in a cohesive zone model by altering the respective strength; the effect of this alteration is illustrated in Fig. 9.

As the bulk strength is increased (through the process zone length ratio $\frac{\ell_{cz}^i}{\ell_{cz}^b} = \frac{\Gamma_i \sigma_b^2}{\Gamma_b \sigma_i^2}$) the contribution of Γ_b to the effective interface toughness disappears and all of the curves collapse to the straight line prediction that represents purely interfacial separation. Hence, the apparent macroscopic toughness in the limit of infinite bulk strength is simply Γ_i , which was confirmed by our simulations.

Fig. 9 illustrates and confirms many of the trends first discovered by Strom and Parmigiani (2014) in their deflection vs. penetration simulations, yet extends it to arbitrary kinking angles. That is, the authors discovered that near the transition region between deflection and penetration, the inactive mechanism begins to act as an energy sink due to competing process zones and delays the active cracking mechanism further. In their work, they clearly illustrate that there exists an elevated

load for deflection near the deflection-to-penetration transition (relative to the He and Hutchinson, 1989a predictions), and conversely an elevated load for penetration near the penetration-to-deflection transition (relative to LFM predictions). Far from the deflection/penetration transition, the authors showed that the results are in near identical agreement with the putative crack analysis of He–Hutchinson in the limit that the interface process zone dominates over the bulk, without including kink sources in the simulation. Both of these trends are identical to what is observed here in Fig. 8: For all phase angles, in the limit that kinking conditions are preferred (dictated by $\tilde{\Gamma}_R < 1$), the results are essentially identical to the He–Hutchinson predictions but without including kink sources.

Conversely, in the limit that delamination is largely preferred (dictated by $\tilde{\Gamma}_R \gg 1$), LFM conditions for interface delamination are recovered over the full range of mode mix for all cases shown in Fig. 9. This is a powerful result, as illustrated in Fig. 9: if one knows a priori that kinking is preferred, then the correct kink angle is selected naturally as an outcome the simulation. Increasing the dimensionless ratio ℓ_{cz}^i/ℓ_{cz}^b simply increases the interface process zone relative to the bulk (as shown in both Figs. 8 and 9), effectively lowering the transition from interface delamination to kinking.

As mentioned, the results in Figs. 8 and 9 illustrate that near the transition between kinking and delamination, the effective toughness of the active mechanism is increased due to damage in the inactive mechanism, which is not realistic for brittle systems. While it would be difficult to show computationally, we hypothesize that continually increasing the cohesive strength would virtually eliminate the competition between process zones and there would be no contribution from the interface toughness to the bulk toughness in the transition region, and vice versa. With that said, there are many material systems where it is known a priori that kinking occurs, in which case the cohesive zone model could be adjusted to suppress delamination entirely. In this limit, as clearly illustrated in Fig. 9, there is virtually no contribution from the interface to the bulk toughness. This is in fact, quite realistic for brittle systems and illustrates that atomistic resolution is not required provided the conditions are far from the transition.

It is worth noting that, despite the approximate nature of the cohesive law for brittle systems, all of the present calculations ensure small fracture process zones relative to the geometry. As such, while the details of the cohesive law are likely to effect the details of process zone interactions, one expects that the trends with relative toughness and strength are reasonable.

5. Conclusions

The results in this paper provide new information regarding the nucleation of kink cracks from an interface, and highlight the role of process zone interactions. We have exploited the unbiased meshing routines of a standard Delaunay triangulation, and demonstrated that at high enough mesh resolution one recovered mesh independent results. The efficient and numerically stable time stepping approach has allowed for broad parameter studies in dimensionless space, effectively relating the required mesh resolution, the cohesive parameters, and the applied macroscopic mode mixity into a compact set of results that can be used for subsequent analysis. The key research findings are:

- For fixed cohesive strength σ_b/E_b , and when the process zones for kinking and delamination are of equal size, the results for both kink direction and critical load for kink nucleation are in excellent agreement with that of He and Hutchinson (1989b). The length scale controlling convergence was shown to be the number of elements per unit length of the fracture length, $\ell_{cz}/h_e = E_b\Gamma/(\sigma^2 h_e)$ (as expected from previous analyses of cohesive zone models), and excellent results were obtained for $\ell_{cz}/h_e > \sim 50$.
- The critical energy release rate is independent of the bulk cohesive strength σ_b/E_b , provided that the bulk fracture length resolution is held constant as σ_b/E_b is changed and enough elements were contained within the process zone.
- The competition between kink nucleation and interface delamination is not always in agreement with the results of He and Hutchinson (1989b,c) due to interacting process zones, with relative process zone size $\frac{\Gamma_i\sigma_b^2}{\Gamma_b\sigma_i^2} = \frac{\ell_{cz}^i}{\ell_{cs}^b}$ controlling the transition. In terms of $\tilde{\Gamma}_R$, the transition criterion between kink nucleation and delamination can be expressed as $\tilde{\Gamma}_R \leq f\left(\psi, \frac{\ell_{cz}^i}{\ell_{cz}^b}\right)$, where f is linear with respect to mode-mix. In contrast, the model of He and Hutchinson for kinking from a putative flaw, which implies that there is no interaction between the fracture process zones, suggests the transition is defined by $\tilde{\Gamma}_R = 1$.
- For all values of the process zone and the toughness ratio, and when kinking or interface delamination are largely preferred (e.g., $\tilde{\Gamma}_R \ll f\left(\psi, \frac{\ell_{cz}^i}{\ell_{cz}^b}\right)$ for kinking and $\tilde{\Gamma}_R \gg f\left(\psi, \frac{\ell_{cz}^i}{\ell_{cz}^b}\right)$ for delamination), it can be generalized that the critical loads for He–Hutchinson crack stability are very similar to those addressing kink nucleation. However, when neither kinking nor delamination are strongly preferred, i.e. $\tilde{\Gamma}_R \sim f\left(\psi, \frac{\ell_{cz}^i}{\ell_{cz}^b}\right)$, the critical loads for kink nucleation or delamination can be much higher due to additional dissipation in the adjacent process zone.

Acknowledgments

This research was financially supported through grant DMR-1105672 from the National Science foundation, grant N00014-13-1-0859 from the Office of Naval Research, grant W911NF-09-0001 through the Institute for Collaborative Biotechnologies from the U.S. Army Research office, and grant DOE/DE-SC0008975 from the Department of Energy. Additional computational

resources were provided by the Center for Scientific Computing at the CNSI and MRL: an NSF MRSEC (DMR-1121053) and NSF CNS-0960316. The content and information presented does not reflect the position or policy of the U.S. government, and no official endorsement should be inferred or implied.

References

- Abanto-Bueno, J., Lambros, J., 2005. Experimental determination of cohesive failure properties of a photodegradable copolymer. *Exp. Mech.* 45 (2), 144–152.
- Abanto-Bueno, J., Lambros, J., 2006. An experimental study of mixed mode crack initiation and growth in functionally graded materials. *Exp. Mech.* 46 (2), 179–196.
- Aoyanagi, Y., Okumura, K., 2009. Stress and displacement around a crack in layered network systems mimicking nacre. *Phys. Rev. E* 79 (6), 066108.
- Azhdari, A., Nemat-Nasser, S., 1996. Energy-release rate and crack kinking in anisotropic brittle solids. *J. Mech. Phys. Solids* 44 (6), 929–951.
- Barenblatt, G.I., 1959. The formation of equilibrium cracks during brittle fracture. general ideas and hypotheses. axially-symmetric cracks. *J. Appl. Math. Mech.* 23 (3), 622–636.
- Bayesteh, H., Mohammadi, S., 2013. Xfem fracture analysis of orthotropic functionally graded materials. *Compos. Part B* 44 (1), 8–25.
- Begley, M.R., Hutchinson, J.W., 2016. *The Mechanics and Reliability of Films, Coatings and Multilayers*, 1. Cambridge University Press, New York, NY.
- Białas, M., Majerus, P., Herzog, R., Mróz, Z., 2005. Numerical simulation of segmentation cracking in thermal barrier coatings by means of cohesive zone elements. *Mater. Sci. Eng. A* 412 (1), 241–251.
- Bilby, B.A., Cardew, G.E., 1975. The crack with a kinked tip. *Int. J. Fract.* 11 (4), 708–712.
- Bilby, B.A., Cardew, G.E., Howard, I.C., 1978. Stress intensity factors at the tips of kinked and forked cracks. In: *Analysis and Mechanics*. Elsevier, pp. 197–200.
- Blackman, B.R.K., Hadavinia, H., Kinloch, A.J., Williams, J.G., 2003. The use of a cohesive zone model to study the fracture of fibre composites and adhesively-bonded joints. *Int. J. Fract.* 119 (1), 25–46.
- Borden, M.J., Verhoosel, C.V., Scott, M.A., Hughes, T.J., Landis, C.M., 2012. A phase-field description of dynamic brittle fracture. *Comput. Methods Appl. Mech. Eng.* 217, 77–95.
- Borg, R., Nilsson, L., Simonsson, K., 2002. Modeling of delamination using a discretized cohesive zone and damage formulation. *Compos. Sci. Technol.* 62 (10), 1299–1314.
- Camacho, G.T., Ortiz, M., 1996. Computational modelling of impact damage in brittle materials. *Int. J. Solids Struct.* 33 (20), 2899–2938.
- Carpinteri, A., Cornetti, P., Barpi, F., Valente, S., 2003. Cohesive crack model description of ductile to brittle size-scale transition: dimensional analysis vs. renormalization group theory. *Eng. Fract. Mech.* 70 (14), 1809–1839.
- Cavalli, M.N., Thouless, M.D., Yang, Q.D., 2004. Cohesive-zone modeling of the deformation and fracture of weld-bonded joints. *Weld. J.* 83 (4), 133–S.
- Cavalli, M.N., Thouless, M.D., Yang, Q.D., 2005. Cohesive-zone modelling of the deformation and fracture of spot-welded joints. *Fatigue Fract. Eng. Mater. Struct.* 28 (10), 861–874.
- Cook, J., Gordon, J.E., 1964. A mechanism for the control of crack propagation in all-brittle systems. *Proc. R. Soc. Lond. A* 282 (1391), 508–520.
- Cook, R.D., et al., 2007. *Concepts and Applications of Finite Element Analysis*. John Wiley & Sons.
- Cotterell, B., Rice, J., 1980. Slightly curved or kinked cracks. *Int. J. Fract.* 16 (2), 155–169.
- Dávila, C.G., Camanho, P.P., de Moura, M.F., 2001. Mixed-mode decohesion elements for analyses of progressive delamination. In: *Proceedings of the 42nd AIAA/ASME/ASCE/AHS/ASC Structures, Structural Dynamics and Materials Conference*, Seattle, WA, 179.
- De Meo, D., Zhu, N., Oterkus, E., 2016. Peridynamic modeling of granular fracture in polycrystalline materials. *J. Eng. Mater. Technol.*
- Dugdale, D.S., 1960. Yielding of steel sheets containing slits. *J. Mech. Phys. Solids* 8 (2), 100–104.
- El-Sayed, S., Sridharan, S., 2002. Cohesive layer models for predicting delamination growth and crack kinking in sandwich structures. *Int. J. Fract.* 117 (1), 63–84.
- Falk, M.L., Needleman, A., Rice, J.R., 2001. A critical evaluation of cohesive zone models of dynamic fracture. *Le J. Phys. IV* 11 (PR5), Pr5–43.
- Fouk III, J.W., Johnson, G.C., Klein, P.A., Ritchie, R.O., 2008. On the toughening of brittle materials by grain bridging: promoting intergranular fracture through grain angle, strength, and toughness. *J. Mech. Phys. Solids* 56 (6), 2381–2400.
- Gerstle, W., Sau, N., Silling, S.A., 2007. Peridynamic modeling of concrete structures. *Nucl. Eng. Des.* 237 (12), 1250–1258.
- Geubelle, P.H., Baylor, J.S., 1998. Impact-induced delamination of composites: a 2d simulation. *Compos. Part B* 29 (5), 589–602.
- Gupta, V., Argon, A.S., Suo, Z., 1992. Crack deflection at an interface between two orthotropic media. *J. Appl. Mech.* 59 (2S), S79–S87.
- Hakim, V., Karma, A., 2009. Laws of crack motion and phase-field models of fracture. *J. Mech. Phys. Solids* 57 (2), 342–368.
- Hamitouché, L., Tarfaoui, M., Vautrin, A., 2008. An interface debonding law subject to viscous regularization for avoiding instability: application to the delamination problems. *Eng. Fract. Mech.* 75 (10), 3084–3100.
- Han, F., Lubineau, G., Azdoud, Y., 2016. Adaptive coupling between damage mechanics and peridynamics: a route for objective simulation of material degradation up to complete failure. *J. Mech. Phys. Solids*.
- Harper, P.W., Hallett, S.R., 2008. Cohesive zone length in numerical simulations of composite delamination. *Eng. Fract. Mech.* 75 (16), 4774–4792.
- Hayashi, K., Nemat-Nasser, S., 1981. Energy-release rate and crack kinking under combined loading. *J. Appl. Mech.* 48 (3), 520–524.
- He, M.-Y., Bartlett, A., Evans, A.G., Hutchinson, J.W., 1991. Kinking of a crack out of an interface: role of in-plane stress. *J. Am. Ceram. Soc.* 74 (4), 767–771.
- He, M.-Y., Hutchinson, J.W., 1989a. Crack deflection at an interface between dissimilar elastic materials. *Int. J. Solids Struct.* 25 (9), 1053–1067.
- He, M.-Y., Hutchinson, J.W., 1989b. Kinking of a crack out of an interface. *J. Appl. Mech.* 56 (2), 270–278.
- He, M.-Y., Hutchinson, J.W., 1989c. Kinking of a Crack Out of an Interface: Tabulated Solution Coefficients. Report MECH-113A. Harvard University, Cambridge, MA.
- Hillerborg, A., Modéer, M., Petersson, P.E., 1976. Analysis of crack formation and crack growth in concrete by means of fracture mechanics and finite elements. *Cem. Concr. Res.* 6 (6), 773–781.
- Hui, C.-Y., Jagota, A., Bennisson, S.J., Londono, J.D., 2003. Crack blunting and the strength of soft elastic solids. In: *Proceedings of the Royal Society of London A: Mathematical, Physical and Engineering Sciences*, 459. The Royal Society, pp. 1489–1516.
- Hutchinson, J.W., Suo, Z., 1992. Mixed mode cracking in layered materials. *Adv. Appl. Mech.* 29 (63), 191.
- Irwin, G.R., 1997. *Plastic Zone Near a Crack and Fracture Toughness*.
- Kang, K.J., 1994. Criteria for kinking out of interface crack. *Eng. Fract. Mech.* 49 (4), 587–598.
- Karihaloo, B.L., Keer, L.M., Nemat-Nasser, S., 1980. Crack kinking under nonsymmetric loading. *Eng. Fract. Mech.* 13 (4), 879–888.
- Kimberley, J., Lambros, J., 2004. Dynamic crack kinking from a pmma/homalite interface. *Exp. Mech.* 44 (2), 158–166.
- Kumar, S., Singh, I.V., Mishra, B.K., Rabczuk, T., 2015. Modeling and simulation of kinked cracks by virtual node xfem. *Comput. Methods Appl. Mech. Eng.* 283, 1425–1466.
- Liechti, K.M., Chai, Y.S., 1991. Biaxial loading experiments for determining interfacial fracture toughness. *J. Appl. Mech.* 58 (3), 680–687.
- Lim, R.K., Pro, J.W., Begley, M.R., Utz, M., Petzold, L.R., 2016. High-performance simulation of fracture in idealized brick and mortar composites using adaptive monte carlo minimization on the gpu. *Int. J. High Perform. Comput. Appl.* 186–199.
- Liu, W., Yang, Q.D., Mohammadzadeh, S., Su, X.Y., 2014. An efficient augmented finite element method for arbitrary cracking and crack interaction in solids. *Int. J. Numer. Methods Eng.* 99 (6), 438–468.
- Liu, W., Yang, Q.D., Mohammadzadeh, S., Su, X.Y., Ling, D.S., 2013. An accurate and efficient augmented finite element method for arbitrary crack interactions. *J. Appl. Mech.* 80 (4), 041033.
- Lo, K.K., 1978. Analysis of branched cracks. *J. Appl. Mech.* 45 (4), 797–802.
- Madenci, E., Colavito, K., Phan, N., 2016. Peridynamics for unguided crack growth prediction under mixed-mode loading. *Eng. Fract. Mech.*

- Madenci, E., Oterkus, E., 2014. *Peridynamic Theory and its Applications*. Springer.
- Miehe, C., Hofacker, M., Welschinger, F., 2010. A phase field model for rate-independent crack propagation: robust algorithmic implementation based on operator splits. *Comput. Methods Appl. Mech. Eng.* 199 (45), 2765–2778.
- Moës, N., Belytschko, T., 2002. Extended finite element method for cohesive crack growth. *Eng. Fract. Mech.* 69 (7), 813–833.
- Motamedi, D., Mohammadi, S., 2012. Fracture analysis of composites by time independent moving-crack orthotropic XFEM. *Int. J. Mech. Sci.* 54 (1), 20–37.
- Needleman, A., 1990a. An analysis of decohesion along an imperfect interface. *Int. J. Fract.* 42 (1), 21–40.
- Needleman, A., 1990b. An analysis of tensile decohesion along an interface. *J. Mech. Phys. Solids* 38 (3), 289–324.
- Nekkanty, S., Walter, M., Shivpuri, R., 2007. A cohesive zone finite element approach to model tensile cracks in thin film coatings. *J. Mech. Mater. Struct.* 2 (7), 1231–1247.
- Nuismer, R.J., 1975. An energy release rate criterion for mixed mode fracture. *Int. J. Fract.* 11 (2), 245–250.
- Parmigiani, J.P., Thouless, M.D., 2006. The roles of toughness and cohesive strength on crack deflection at interfaces. *J. Mech. Phys. Solids* 54 (2), 266–287.
- Pathak, H., Singh, A., Singh, I.V., 2013. Fatigue crack growth simulations of bi-material interfacial cracks under thermo-elastic loading by extended finite element method. *Eur. J. Comput. Mech.* 22 (1), 79–104.
- Prasad, S., Carlsson, L.A., 1994a. Debonding and crack kinking in foam core sandwich beams I. Analysis of fracture specimens. *Eng. Fract. Mech.* 47 (6), 813–824.
- Prasad, S., Carlsson, L.A., 1994b. Debonding and crack kinking in foam core sandwich beams II. Experimental investigation. *Eng. Fract. Mech.* 47 (6), 825–841.
- Pro, J.W., Lim, R.K., Petzold, L.R., Utz, M., Begley, M.R., 2015a. Gpu-based simulations of fracture in idealized brick and mortar composites. *J. Mech. Phys. Solids* 80, 68–85.
- Pro, J.W., Lim, R.K., Petzold, L.R., Utz, M., Begley, M.R., 2015b. The impact of stochastic microstructures on the macroscopic fracture properties of brick and mortar composites. *Extreme Mech. Lett.* 5, 1–9.
- Rabczuk, T., Zi, G., Gerstenberger, A., Wall, W.A., 2008. A New Crack Tip Element for the Phantom-node Method with Arbitrary Cohesive Cracks.
- Rice, J.R., 1979. *The Mechanics of Earthquake Rupture*. Division of Engineering, Brown University.
- Shewchuk, J.R., 1996. Triangle: Engineering a 2d quality mesh generator and delaunay triangulator. In: *Applied Computational Geometry Towards Geometric Engineering*. Springer, pp. 203–222.
- Shewchuk, J.R., 2002. Delaunay refinement algorithms for triangular mesh generation. *Comput. Geom.* 22 (1), 21–74.
- Silling, S.A., 1998. Reformulation of Elasticity Theory for Discontinuous and Long-range Forces. SAND98-2176. Sandia National Laboratories, Albuquerque, NM.
- Silling, S.A., Lehoucq, R.B., 2008. Convergence of peridynamics to classical elasticity theory. *J. Elast.* 93 (1), 13–37.
- Strom, J.L., Parmigiani, J.P., 2014. Transition of crack path at bi-material interfaces. *Eng. Fract. Mech.* 115, 13–21.
- Tada, H., Paris, P.C., Irwin, G.R., 1973. *The Stress Analysis of Cracks*. Handbook, Del Research Corporation.
- Turon, A., Davila, C.G., Camanho, P.P., Costa, J., 2007. An engineering solution for mesh size effects in the simulation of delamination using cohesive zone models. *Eng. Fract. Mech.* 74 (10), 1665–1682.
- Tvergaard, V., 1990. Effect of fibre debonding in a whisker-reinforced metal. *Mater. Sci. Eng. A* 125 (2), 203–213.
- Tvergaard, V., Hutchinson, J.W., 1992. The relation between crack growth resistance and fracture process parameters in elastic-plastic solids. *J. Mech. Phys. Solids* 40 (6), 1377–1397.
- Wu, C.H., 1978a. Elasticity problems of a slender z-crack. *J. Elast.* 8 (2), 183–205.
- Wu, C.H., 1978b. Fracture under combined loads by maximum-energy-release-rate criterion. *J. Appl. Mech.* 45 (3), 553–558.
- Wu, C.H., 1978c. Maximum-energy-release-rate criterion applied to a tension-compression specimen with crack. *J. Elast.* 8 (3), 235–257.
- Wu, C.H., 1979. Explicit asymptotic solution for the maximum-energy-release-rate problem. *Int. J. Solids Struct.* 15 (7), 561–566.
- Xie, D., Waas, A.M., 2006. Discrete cohesive zone model for mixed-mode fracture using finite element analysis. *Eng. Fract. Mech.* 73 (13), 1783–1796.
- Xu, X.-P., Needleman, A., 1994. Numerical simulations of fast crack growth in brittle solids. *J. Mech. Phys. Solids* 42 (9), 1397–1434.
- Zavattieri, P.D., Hector Jr, L.G., Bower, A.F., 2008. Cohesive zone simulations of crack growth along a rough interface between two elastic-plastic solids. *Eng. Fract. Mech.* 75 (15), 4309–4332.
- Zhu, F., Zhao, J., 2016. A peridynamic approach for numerical modelling of sand grain crushing. In: *The 20th Annual Conference of HKSTAM 2016 The 12th Shanghai-Hong Kong Forum on Mechanics and Its Application*, p. 31.